Abnormal Grain Growth and Pseudoelasticity of Industrially Processed Fe–Mn–Al–Ni Shape Memory Alloy Joined by Metal Inert Gas Welding

VINCENT FABIAN VIEBRANZ ⓘ, ANDRÉ BAUER ⓘ, THOMAS HASSEL ⓘ, THOMAS NIENDORF ⓘ, and HANS JÜRGEN MAIER ⓘ

The effect of metal inert gas welding on the microstructure, abnormal grain growth and the pseudoelastic properties of industrially processed Fe–Mn–Al–Ni shape memory alloy sheets were studied. Square-butt welds were manufactured using similar filler material. The influence of alternating mean arc linear energy on the microstructure of the individual zones is shown. A correlation between the process parameters, the associated heat input, the grain morphology and the α/γ-ratio could be deduced. As the mean arc linear energy increases, the α/γ-ratio in the fusion zone and the heat-affected zone increases. To evaluate the influence of the welding process on abnormal grain growth, a post-weld cyclic heat-treatment was carried out. Although no loss of major alloying elements in the fusion zone was observed after welding, metal inert gas welding has a significant effect on grain growth upon cyclic heat treatment. While abnormal grain growth occurred in the base material, a polycrystalline microstructure characterized by significantly smaller grain sizes was visible in the former fusion zone. Incremental strain tests revealed severe plastic deformation near the grain boundaries in the former fusion zone. However, the grain boundaries of the bamboo-like grown grains in the base material turned out to be more critical for structural failure.

I. INTRODUCTION

IRON-BASE shape memory alloys (SMAs) can accommodate strains *via* a reversible martensitic transformation (MT), exceeding the elastic deformation of conventional structural materials. Given the low material costs and the processing properties, Fe-SMAs are potential candidate materials for damping applications in civil engineering.[1–3] Compared to other SMAs, such as NiTi, a number of Fe-SMAs are characterized by a lower temperature dependence of the MT with a Clausius-Clapeyron relation of 0.53 MPa K^{-1}.[4] According to the ASTM 709 Standard Specification for Structural Steel for Bridges, the lowest operation temperature for bridge applications is set to 222 K.[2]

This limits the application of NiTi-SMA, whereas Fe-SMAs can show pseudoelasticity down to 123 K.[4]

Pseudoelasticity in the quaternary Fe–Mn–Al–Ni alloy is caused by a reversible MT from an α parent phase (A2, bcc), referred to as austenite, to a martensitic γ'-phase (A1, fcc).[4,5] Here, the α/γ equilibrium is attributed to a change of the magnetic contribution to the Gibbs energy. For increasing Mn and Al contents, a decrease of the magnetic contribution can be observed, lowering the Curie temperature T_C^α of the α-phase and ultimately resulting in a γ-solvus temperature near 1430 K. Stabilization of the γ-phase down to room temperature is achieved.[4]

While for single crystalline and oligocrystalline microstructures of $Fe_{43.5}Mn_{34}Al_{15}Ni_{7.5}$ pseudoelastic reversibility of up to 10 pct is reported,[4–6] the polycrystalline state is characterized by pronounced unrecovered strains ε_{irr} during cyclic loading and rapid functional degradation.[7–9] Fe–Mn–Al–Ni features a strong dependence of the transformation strain and the critical transformation stress σ_c on the crystallographic orientation. This results in functional degradation caused by internal stresses between transformed grains with different orientations, especially in the vicinity of triple grain boundary junctions.[10–13] The shape memory effect (SME) of the polycrystalline state can be

VINCENT FABIAN VIEBRANZ, THOMAS HASSEL, and HANS JÜRGEN MAIER are with the Institut für Werkstoffkunde (Materials Science), Leibniz Universität Hannover 30823, Garbsen, Germany. Contact e-mail: viebranz@iw.uni-hannover.de ANDRÉ BAUER and THOMAS NIENDORF are with the Institut für Werkstofftechnik (Materials Engineering), Universität Kassel 34125, Kassel, Germany.

improved by abnormal grain growth (AGG) *via* a cyclic heat-treatment (CHT), leading to a reduction of the overall grain boundary surface and the amount of unfavorably oriented grains.[4,5,7,14] Upon transformation from the α single-phase region at high temperatures to the α + γ two-phase region at lower temperatures (as shown in References 5, 14) grain growth is promoted and grains can span entire specimen cross sections.[4,5,7,14]

The crystallographic orientation dependence both of σ_c and the reversibility of the MT lead to a huge effect of the grain orientation on the resulting pseudoelastic properties. In the twinned and detwinned state of the martensite, the $\langle 100 \rangle$ direction exhibits the highest theoretical transformation strain.[15–17] However, detwinning results in loss of recoverability.[18] Less favorable transformation strains are associated with the $\langle 111 \rangle$ direction, combined with an increase of $d\sigma_c/dT$ to 2.05 MPa K^{-1} in $\langle 111 \rangle$ oriented single crystals, as the transformation strain is related to the Clausius-Clapeyron relation.[17] In contrast to the theoretically determined values, the $\langle 123 \rangle$ direction shows superior, fully reversible transformation strain in experiments[16,17] and orientations near $\langle 101 \rangle$ retain the twinned martensite eventually leading to less ε_{irr}.[18]

Several studies addressed weldability and the interrelationship between process parameters and microstructure in Fe-SMAs, which were expected to be similar to commercially available high-alloyed steels. Specifically, a major α fraction in the fusion zone (FZ) with γ precipitation along the grain boundaries has been reported,[19–25] whereas the heat-affected zone (HAZ) is characterized by a large fraction of the γ-phase. Especially during tungsten inert gas welding the HAZ can be described by two distinct regions. Due to significantly lower temperatures, transformation from α → γ takes place in the outer region, directly connected to the base material (BM), increasing the γ fraction. The second region adjacent to the FZ is characterized by an equiaxed microstructure with a higher γ fraction relative to the FZ.[23] While a relationship between grain growth with increasing heat input is evident for the FZ, this is not observable for the HAZ.[23] During welding with higher heat input, the α/γ-ratio increases in the FZ,[21,23] while it decreases in the HAZ.[23]

Concerning an industrial application of Fe-SMA damping devices, in particular $Fe_{43.5}Mn_{34}Al_{15}Ni_{7.5}$, commercially established fusion processes and their impact on the pseudoelasticity (PE) needs to be investigated closer. Since the PE strongly depends on the phases and grain diameters present, post weld heat-treatments need to be considered with respect to later applications. The present study addresses the interplay between welding, AGG and PE. For this purpose, metal inert gas (MIG) welding was employed to fuse industrially produced $Fe_{43.5}Mn_{34}Al_{15}Ni_{7.5}$ with similar filler material. To understand the effect of the mean arc linear energy on the formed phases and the resulting microstructure, square butt welds were carried out. Subsequent heat-treatment processes, especially AGG, were used to establish a microstructure beneficial for exploiting PE. To investigate the correlation between the welding processes, the grain growth during AGG and the PE, optical microscopy (OM), scanning electron microscopy (SEM), X-ray diffraction (XRD) and *in-situ* incremental strain tests (ISTs) were employed.

II. EXPERIMENTAL

A. *Materials and Processing*

Hot-rolled $Fe_{43.5}Mn_{34}Al_{15}Ni_{7.5}$ sheets with a thickness of 2 mm were produced by thyssenkrupp Steel Europe AG (Duisburg, Germany) using industrial process routes on a laboratory scale. 2 × 2 mm strips were cut from the sheet material by abrasive water jet cutting. These strips served as starting material for the similar filler material. In order to reduce dislocation density introduced during the hot rolling process and to ensure a homogeneous chemical composition over the entire cross-section, the strips were first solution annealed under an Ar atmosphere at 1473 K for 5 minutes, followed by air-cooling to room temperature. Subsequently, a second heat-treatment at 1073 K for 5 minutes followed by air-cooling was carried out to generate a microstructure being characterized by a high amount of the ductile γ-phase. Before cold drawing any scaling was removed with abrasive fleece (Hoffmann Group, Munich, Germany) followed by cleaning with ethanol (CVH, 99 pct). XRD phase analysis were performed on a BRUKER D8 (Bruker Corporation, Billerica) in an angular range from 45 to 120 deg 2Θ and an irradiated spot diameter of 0.3 mm. Co-K_α radiation (45 kV; 35 mA) was used to determine the phases present prior to heat-treatment and subsequent to each step on sections cut perpendicular to the drawing direction. The sequence of the heat-treatment and the cold drawing is illustrated in Figure 1. To investigate strain hardening caused by drawing, wires with a final diameter of 1.80, 1.60, 1.40 and 1.20 mm were mechanically strained on a Z100 materials testing machine (ZwickRoell AG, Ulm, Germany).

B. *Welding*

Specimens 60 mm long and 40 mm wide were cut by abrasive water jet cutting and subsequently cleaned by sandblasting and rinsed with ethanol to remove any residues. The specimens were joined with square butt welds parallel to the rolling direction, maintaining a 1 mm gap (*i.e.*, half of the sheet thickness). Welding with this specific geometry ensures that the loading direction during the ISTs is aligned parallel to the solidification direction in the FZ. A grooved and internally cooled (approx. 289 K) copper plate was used as weld bead support. The welds were produced with an Abicor Binzel ROBO WH W 500 torch (Alexander Binzel Schweisstechnik GmbH & Co. KG, Buseck, Germany) and a Carl Cloos GLC 303 PA/3 welding rectifier (Carl Cloos Schweisstechnik GmbH, Haiger, Germany) with
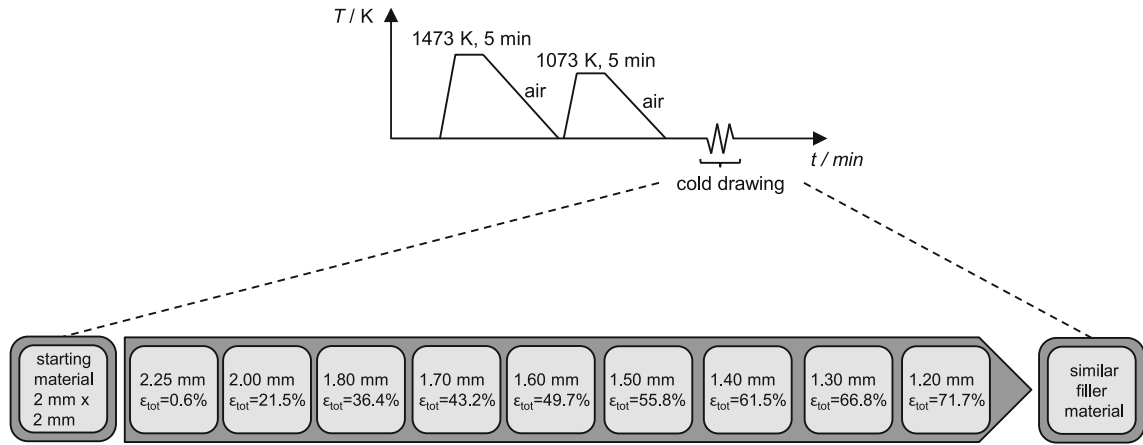
Fig. 1—Thermo-mechanical history of the wires; for each iteration during the cold drawing process the wire diameter as well as the accumulated area reduction ε_{tot} are given.

Table I. Welding Parameters Used in the Present Study; Contact Tube to Working Distance of 12 mm; Torch Angle of 90 deg; * Marks the Parameter Set Used for Cyclic Heat-Treatment and Mechanical Testing

	Conditions			
Welding Shape	Wire Feed v_w (m min^{-1})	Welding Speed v (mm min^{-1})	Filler Material	Shielding Gas
Square Butt Weld	2.5	300	similar ($\varnothing = 1.2$ mm)	70/30 Ar/He (12 L min^{-1})
	3*	500*		
	3	700		
	3.5	1000		

an internal constant voltage characteristic. The torch was mounted on a guiding system with stepper motors to ensure a constant welding speed, torch angle (90 deg) and contact tube to working distance (12 mm). As shown in Reference 24, a change of the shielding gas composition affects the temperature-time path upon cooling, which in turn leads to an altered γ-phase precipitation. Using a gas composition of 70/30 Ar/He led to less susceptibility to cracking, thus, the same composition was used in the present study. The volume flow of the Ar and He (Ar: ARCAL™ Prime (99.998 pct), He: Lasal 4 (99.996 pct); Air Liquide S.A., Paris, France) was kept constant at 12 L min^{-1} during welding. The welding parameters are listed in Table I. By varying the welding speed between 300 and 1000 mm min^{-1} and the wire feed between 2.5 and 3.5 m min^{-1}, the effect of the mean arc linear energy on the microstructure was investigated. The resulting current was recorded using a Chauvin Arnoux PAC22 clamp meter (CHAUVIN ARNOUX, Paris, France), while the voltage was recorded between the torch and the work piece. A National Instruments NI USB-6361 A/D converter (National Instruments, Austin) with a rate of 5×10^4 samples per second was used to record the data, which were visualized using MATLAB software (Mathworks, Natick). For details see Reference 26.

C. Post-weld Heat-Treatment

To study the impact of the welding process on AGG, a CHT was carried out for the parameter set highlighted in Table I. In this context, $24 \times 3 \times 2$ mm bar specimens and tensile specimens with a gauge length of 18 mm and a cross-section of 1.5×1.8 mm were used. The specimens were extracted by electric discharge machining perpendicular to the weld direction so that the fusion zone was located in the middle of the specimens. The bar specimens were ground at the cutting surfaces to remove the machining-affected surface layer. The top and bottom side of the bar specimens, including the weld upset and the root sag of the weld seam, were not ground. The tensile specimens were ground down to 5 μm at all sides to minimize surface and geometric influences on the grain growth behavior. To prevent oxidation during the CHT, the specimens were sealed into quartz tubes under Ar atmosphere. The CHT was carried out between the α single-phase region at 1498 K and the $\alpha + \gamma$ two-phase region at 1173 K. A total of three heat-treatment cycles were carried out during the CHT, each with a dwell time of 60 minutes at 1498 K and 15 minutes at 1173 K. The heating and cooling ramps were 5 K min^{-1}. Finally, the specimens were quenched at air for 40 seconds in order to avoid the formation of martensite,[21] directly followed by an aging heat treatment at 498 K for 5 hours.

D. *Chemical Composition*

Prior to welding, the chemical composition of the base material was determined by inductively coupled plasma optical emission spectroscopy (ICP-OES, SPECTRO CIROS VISION EOP; SEPCTRO Analytical Instruments, Kleve, Germany). Energy dispersive spectroscopy (EDS) line scans for determination of the chemical composition of the HAZ and FZ were carried out in a VISITEC MIRA XV SEM (VisiTec Microtechnik, Grevesmühlen, Germany) equipped with a backscattered electron (BSE) detector (ELLCIE, Grevesmühlen, Germany) and an EDS detector (Thermo Fisher Scientific, Waltham). Light elements such as H, N, and O were analyzed by melting gas extraction (TCH 600; LECO, Mönchengladbach, Germany). For this purpose, specimens with 10 mm length and 3 mm width were sectioned using abrasive water jet cutting from the FZs as well as from the BM. To prevent oxidation affecting the O content, prior to testing each specimen was etched with 2 molar HCl (ROTH, 37 pct) and submerged in ethanol after rinsing.

E. *Microstructural Characterization*

Cross-sections were used for metallographic examination. First, the specimens were ground and polished (0.06 μm) employing a VIBROMET 2 (Buehler, Echterdingen, Germany), followed by etching with a solution of 2 pct HNO_3 (ROTH, 68 pct pure) and ethanol. OM was carried out using a ZEISS OYLUMPUS BX53M (Carl Zeiss AG, Oberkochen, Germany) microscope. For measurements of the grain major axis the software OLYUMPUS Stream (Carl Zeiss AG, Oberkochen, Germany) and Fiji (open-source platform[27]) were used. XRD phase analysis was carried out to measure the phases present after welding. Subsequently to CHT, another set of cross-sections was prepared, which were ground and polished. Prior to OM, employing a Keyence VHX 7100 (Keyence GmbH, Neu-Isenberg, Germany), the specimens were etched. To determine the crystallographic orientation of the grains, present in the gauge length of the tensile specimens after CHT, electron-backscatter diffraction (EBSD) measurements were carried out.

F. *Mechanical Characterization*

The ISTs, accompanied by digital OM (Keyence VHX-600: Keyence GmbH, Neu-Isenberg, Germany), were performed at room temperature on a servo-hydraulic testing machine (Schenk RoTec GmbH, Darmstadt, Germany) equipped with a 5 kN load cell. The ISTs were carried out in displacement control with a constant crosshead displacement of 5 $\mu m\ s^{-1}$. Strains were measured using an extensometer with a gauge length of 12 mm directly attached at the gauge length. The ISTs were performed in steps of 2 pct strain up to failure. Images of the specimen surfaces were taken in the loaded and unloaded condition for each step and after failure.

III. RESULTS AND DISCUSSION

A. *Wire Drawing*

Changes of the α and γ-phase fractions during heat-treatment of the initial 2×2 mm material are shown in Figure 2. Considering the relative intensities in Figure 2(a), the material is characterized by a large γ fraction prior to heat-treatment, while a minor content of the α-phase is present. Due to the hot-rolled condition of the BM, the initial filler material was first solution annealed to minimize residual strain and recover already formed dislocations upon processing. The treatment at 1473 K led to an increase of the α fraction, indicated by the higher intensity of the (110)α peak in Figure 2(b) compared to Figure 2(a); effects of texture are not taken into account at this point. Since an overall low amount of α-phase is beneficial, so that the $\alpha \rightarrow \gamma'$ transformation and the associated strain hardening are minimized, a second heat-treatment was conducted to prevent failure during cold drawing. Figure 2(c) shows the diffraction pattern after the 1073 K heat-treatment. As the selected temperature is below the γ solvus temperature of 1430 K,[4] the $\alpha \rightarrow \gamma$ transformation takes place lowering the amount of the α-phase and therefore leading to a lower relative intensity. The transformation during the heat-treatment is also illustrated by the OM images of the corresponding states. While in Figure 2(d) the γ-phase dominates, an increase of the α-phase after solution annealing becomes apparent in Figure 2(e). After the second treatment at 1073 K the γ-phase fraction increases again.

The strain hardening during cold drawing was investigated by tensile tests of the wires. Figure 3 illustrates the mean tensile strength for the BM as well as for the wires with diameters of 1.8, 1.6, 1.4 and 1.2 mm. Due to the deformation upon cold drawing, strain hardening and irreversible MT occurs, resulting in tensile strengths exceeding the values found for the BM. Since no specimen failed prematurely during the tensile tests, no necking was assumed to occur during cold drawing.

B. *Mean Arc Linear Energy*

By recording the welding current and voltage, the correlation between heat input and resulting microstructure can be investigated. Figures 4 and 5 show the measured voltage U and current I, and the calculated power $P = U\,I$ during the welding for a time span of 0.5 seconds. In accordance to the standard DIN EN 1011-1, the mean arc linear energy can be determined as $Q = (U\,I\,\eta)/v$ ($\eta = 0.8$), where U, I and v are arc voltage, current and welding speed. To obtain the mean arc linear energy for each weld, the mean arc voltage $\overline{U}$ and arc current $\overline{I}$ were determined. The calculated values are given in Figures 4 and 5. Higher wire feed rates result in an increase of the arc's power P, and therefore the deposition rate is increased. The welding speed v can be increased to counteract weld failures during processing. Due to the increased v, the mean arc linear energy Q is lowered despite the higher P. Additionally, the increase of the arc's power results in fewer short circuit
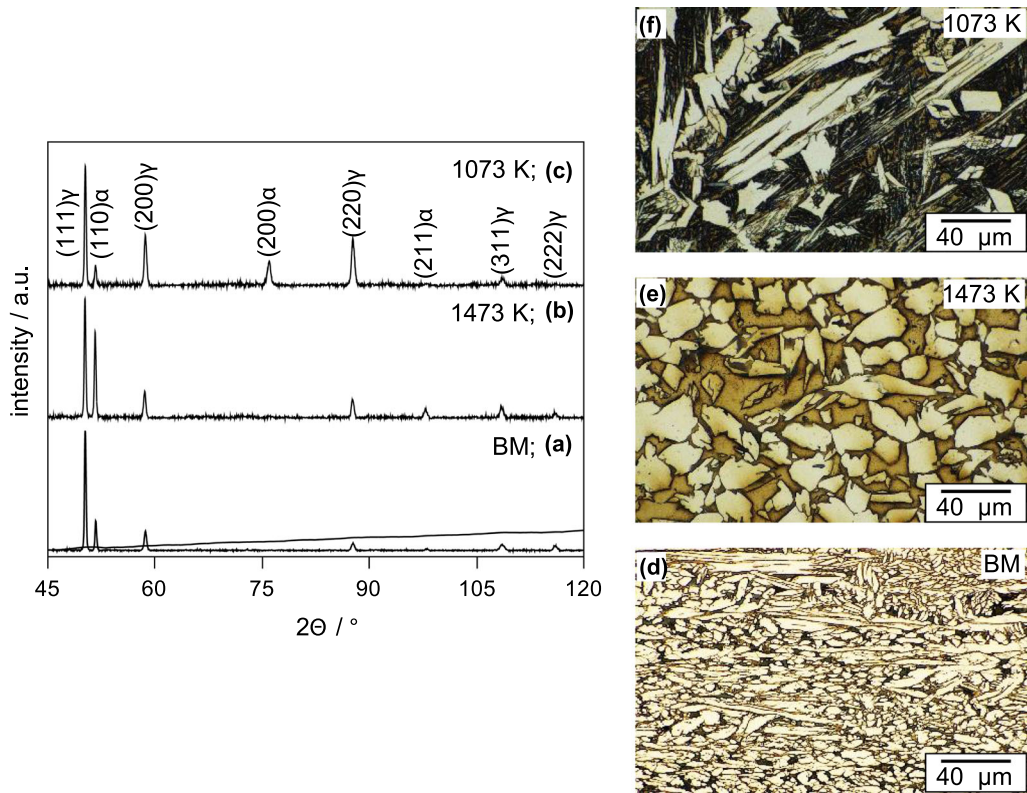
Fig. 2—Diffraction patterns with subtracted background (dotted line in *a*) of the initial 2 × 2 mm filler material: (a) prior to heat-treatment, (b) heat-treated for 5 minutes at 1473 K followed by air cooling, (c) heat-treated for 5 minutes at 1073 K followed by air cooling; corresponding micrographs are shown in (d) through (f).
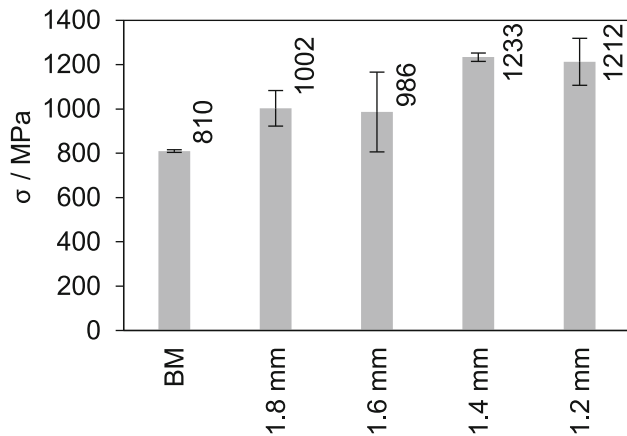

Fig. 3—Mean tensile strength of the base material (BM) as well as for the wires with diameters of 1.8, 1.6, 1.4, and 1.2 mm.

events and larger droplets. Figure 6 illustrates the OM images of the welds. For all parameter sets a defect free fusion was achieved. While during all welds a full penetration was achieved, in Figure 6(a) the molten material forms solidified droplets (icicles). As the mean arc linear energy decreases, while the arc's power increases, the droplet formation is less pronounced and the weld seam width broadens.

C. Chemical Composition

The mean chemical composition of the BM was determined as $FeMn_{32.3}Al_{13.9}Ni_{7.5}$ (at. pct, Fe balance) by ICP-OES, which differs only slightly from the nominal composition of $Fe_{43.5}Mn_{34}Al_{15}Ni_{7.5}$ given by the supplier thyssenkrupp Steel Europe. To investigate element loss during the welding process in more detail, EDS line scans of the BM, HAZ and FZ of the welds with $Q = 267$ J mm^{-1} and $Q = 213$ J mm^{-1} were carried out (Figure 7). EDS data typically have an absolute error of 2 to 5 pct, while relative changes can be detected with much higher resolution. To evaluate the changes in the chemical composition induced by welding only the latter aspect is important. No significant loss could be detected in the distinct zones of the welds, which indicates that alloying element loss during welding was negligible.

The H, N, and O contents determined by melting gas extraction are shown in Figure 8. While for the main alloying elements no significant variation between the distinct zones relative could be detected, major differences occurred for the minor elements. When the nitrogen content is compared between the BM and the welds with different heat input, it appears that during processing the nitrogen content is lowered, especially for processes with high arc power and low Q. As reported in References 28, 29, during the droplet transition and due
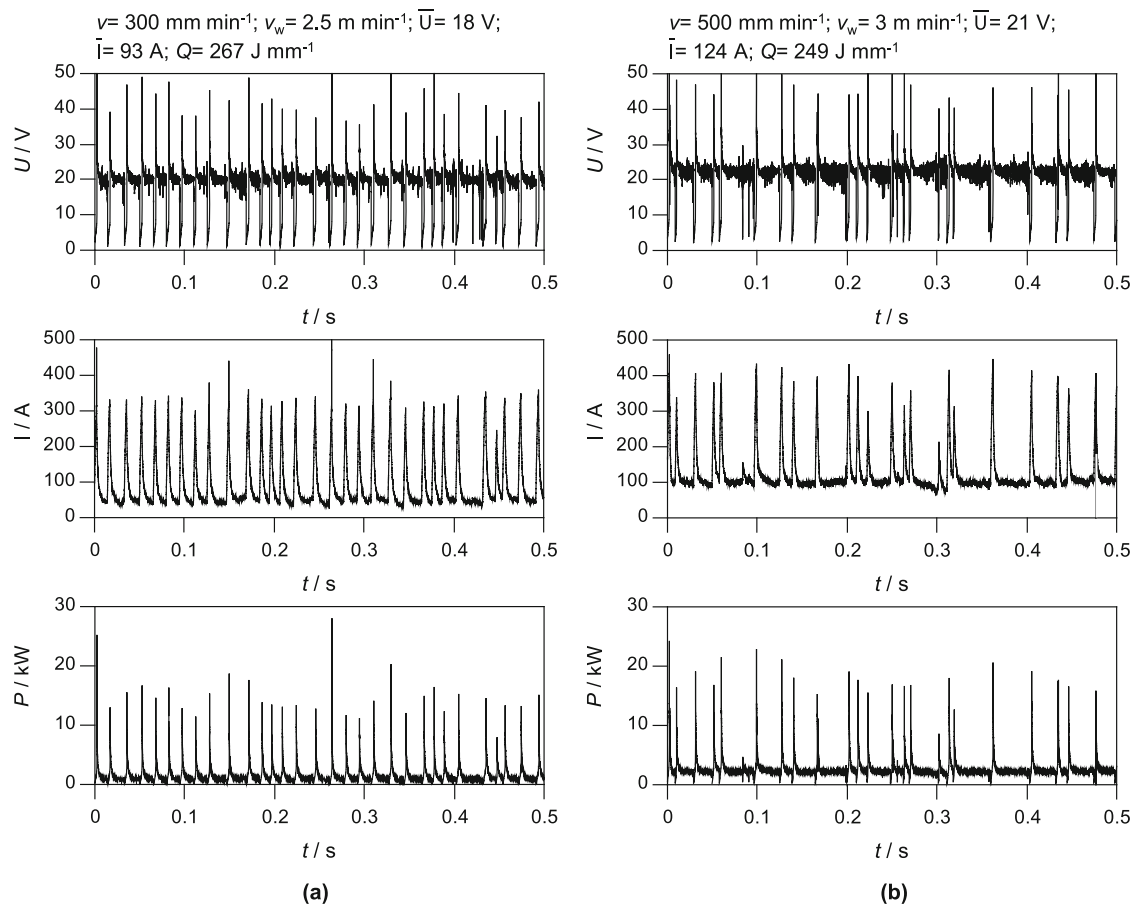
Fig. 4—Measured voltage and current during welding with (*a*) $v = 300$ mm min^{-1}, $v_w = 2.5$ m min^{-1} and (*b*) $v = 500$ mm min^{-1}, $v_w = 3$ m min^{-1}; the calculated mean voltage $\overline{U}$, mean current $\overline{I}$ and mean linear arc energy Q are given.

to the lower solubility of the nitrogen in the molten filler material, desorption takes place lowering the N content. Especially for temperatures above 1773 K, the solubility of N in the molten material drops significantly.[29] A decrease of the H content was not detected. Despite the deoxidation of the surface by etching, neither an increase nor a decrease of the O content could be detected. However, as indicated by the varying mean oxygen content for the individual specimens, the oxygen content is affected by the affinity of manganese and iron to form oxides. Since the phase stability upon cooling is affected by the alloying elements, particularly relevant for the mechanism promoting AGG, the loss of minor elements during welding might cause different thermodynamically conditions when post weld heat-treatments are applied leading to different grain growth rates in the BM and FZ.

D. Characterization of the As-Welded State

In order to investigate the influence of the welding process onto the post-weld heat-treatment and PE, the grain morphology and phases present in the FZ and HAZ were characterized. Figure 9 shows the cross-sections of the FZs with altering Q. While in Figures 9(b) and (d) through (e) the γ-phase by far dominates, the

α-phase also contributes a significant fraction in Figure 9(c). Upon cooling the γ-phase mainly forms at the grain boundaries. However, further $\alpha \rightarrow \gamma$ transformation takes place, eventually resulting in γ grains growing inside the primarily solidified α grains. Since in Figure 9(c) the γ-phase has mainly formed along the grain boundaries and only small fractions are identifiable inside the grains, a higher cooling rate compared to (b) and (d) through (e) can be assumed. Despite the higher Q, material transition during the weld as well as the welding speed and the arc shape finally affect the cooling rate, which may have led to the higher α-phase content in Figure 9(c). It has to be noted, that the heat input can be characterized by the linear arc energy Q as well as the droplet transition, torch distance and shielding gas composition during welding. In the present study the measurement of Q is used to correlate the formed phases with the heat input during welding for the specific welding setup. The employed cooled weld bead support served as a heat sink, to achieve a narrow HAZ and suppress excessive γ-phase precipitation. Heat accumulation during welding may cause broader HAZs, leading to a larger area influenced by the welding process. An influence of different cooling strategies onto the formed phases needs to be investigated in future studies.
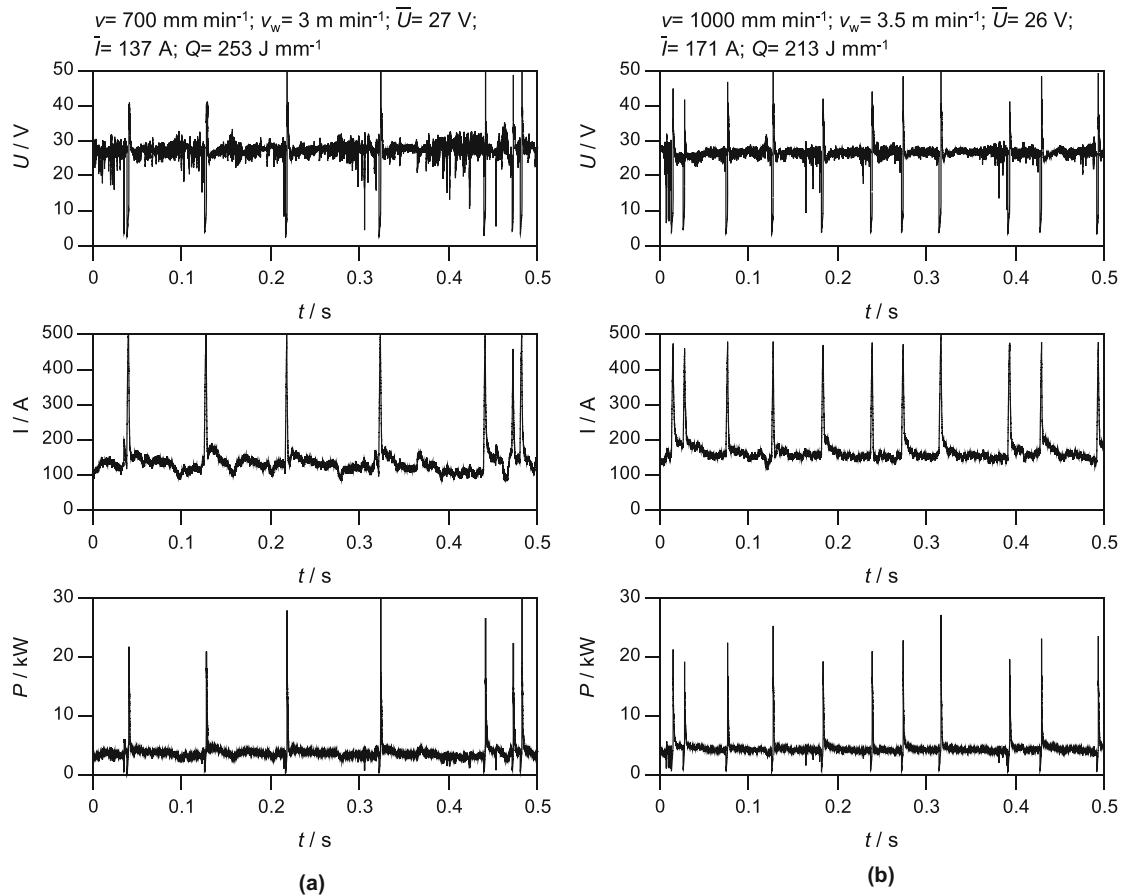
Fig. 5—Measured voltage and current during the welds with (a) $v = 700$ mm min^{-1}, $v_w = 3$ m min^{-1} and (b) $v = 1000$ mm min^{-1}, $v_w = 3.5$ m min^{-1}; the calculated mean voltage $\overline{U}$, mean current $\overline{I}$ and mean linear arc energy Q are given.

As reported in References 21, 23 the α fraction in the FZ increases with increasing heat input. To verify this assumption, XRD measurements were carried out. The diffraction patterns obtained for the BM and the FZ of the welds with $Q = 267$ J mm^{-1} and $Q = 213$ J mm^{-1}, respectively, are shown in Figure 10. For both welds the relative intensity of the (110)α peak is higher than in the BM. When the weld with $Q = 267$ J mm^{-1} [Figure 10(b)] is compared to the weld with $Q = 213$ J mm^{-1} [Figure 10(c)], a decrease of the relative intensity of the α-phase can be identified with decreasing Q. This is in agreement with the observations in References 21, 23. When the diffraction patterns of the FZs in Figure 10 are compared with those in Reference 23, a higher γ fraction is detectable for the MIG process. The altered γ precipitation induced by the change of welding process, may be caused by a different temperature-time-path due to an alternation of the weld pool geometry. The diffraction patterns of Figures 10(b) and (c) indicate hardly any pronounced texture caused by epitaxial growth during solidification upon cooling of the melt pool.

In addition to the phase fractions, grain growth is also affected by the heat input.[23] The major axis of the grains was measured at higher magnifications than

shown in Figure 9. When the major axis of the grains in the FZs are compared, an increase of the mean major axis from 485 μm [Figure 9(b)] to 625 μm [Figure 9(c)] becomes apparent. With further decrease of Q, the major axis decreases again, from 420 μm in Figure 9(d) to 370 μm in Figure 9(e). While the increase of the major axis with increase of the heat input is consistent with Reference 23, the decrease of the mean major axis with further increase of the heat input might be caused by similar events of nucleation ahead of the solidification front instead of epitaxial growth as observed during columnar to equiaxed transition. In addition, fragmentation of fast-growing dendrites may also lead to new nucleation sites competing with the already grown grains, lowering the mean major axis.

Figure 11 shows OM images of the HAZs. While the FZ is characterized by a large γ fraction with indistinguishable α grains, in all HAZs the α grains can be identified. Further, γ precipitation took place along the grain boundaries and only a small proportion of γ-phase inside the grains can be determined. While in Reference 23 a larger γ fraction in the HAZ than in the FZ was reported, in the present study the opposite was observed. Grain growth associated with increasing heat input was not evident for the HAZ. The mean major
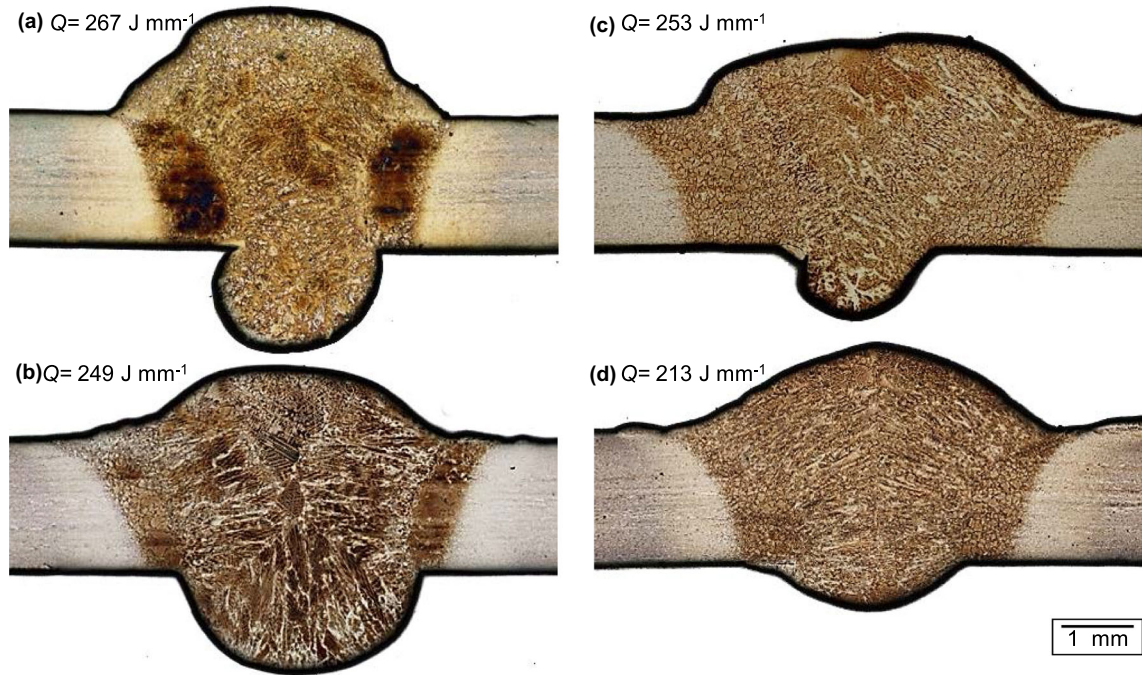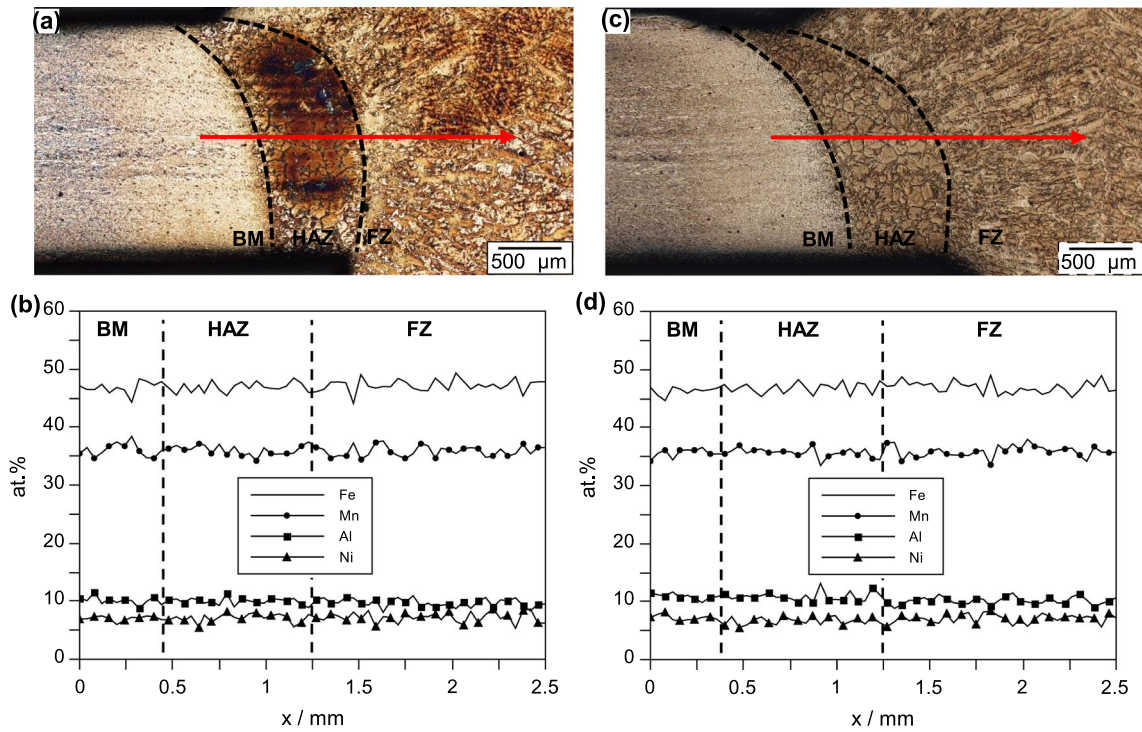
Fig. 6—OM of polished and etched cross-sections of the square butt weld with $v = 300$ mm min^{-1}, $v_w = 2.5$ m min^{-1}, $Q = 267$ J mm^{-1} in (a), $v = 500$ mm min^{-1}, $v_w = 3$ m min^{-1}, $Q = 249$ J mm^{-1} in (b), $v = 700$ mm min^{-1}, $v_w = 3$ m min^{-1}, $Q = 253$ J mm^{-1} in (c) and $v = 1000$ mm min^{-1}, $v_w = 3.5$ m min^{-1}, $Q = 213$ J mm^{-1} in (d).

Fig. 7—OM of polished and etched cross-section of the square butt weld with $v = 300$ mm min^{-1}, $v_w = 2.5$ m min^{-1}, $Q = 267$ J mm^{-1} in (a); (b) chemical composition determined by EDS line-scans along the red arrow in (a); OM of polished and etched cross-section of the square butt weld with $v = 1000$ mm min^{-1}, $v_w = 3.5$ m min^{-1}, $Q = 213$ J mm^{-1} in (c); (d) chemical composition determined by EDS line-scans along the red arrow in (c) (Color figure online).
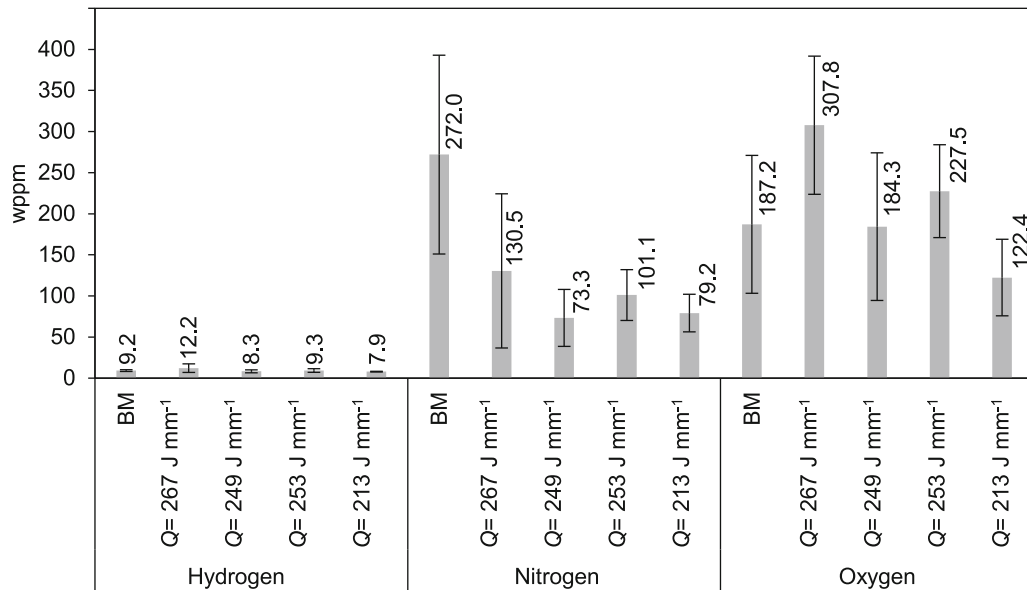
Fig. 8—Analysis of the minor elements H, N, and O by melting gas extraction; specimens were taken from the BM as well as from the FZ for each weld; mean wppm is given.

axis for all process parameters ranges from 120 to 145 μm. In contrast to the FZ, γ' martensite could be identified inside the α grains. An overall low fraction of γ-phase, compared to the FZ, leads to higher internal stresses and therefore causes MT.

The phases present in the HAZ were investigated by XRD. Figure 12 shows the diffraction patterns of the BM and of the HAZ of the weld with $Q = 267$ J mm^{-1} and $Q = 213$ J mm^{-1}, respectively. Overall, a higher relative intensity of the (110)α peak in the HAZ compared to the FZ becomes apparent (texture effects are not considered at this point). Since no alloying element loss was detected, the differences in γ precipitation in the FZ and HAZ can mainly be attributed to differences in the overall thermal history and heat accumulation in the weld pool.

When the boundary between the HAZ and the FZ is observed [cf. Figure 11(b)] a transition from an equiaxed microstructure to an uniaxial-elongated microstructure is evident. In the center of the weld seam a clear columnar microstructure is present. A locally unidirectional temperature gradient leads to an equiaxed microstructure, while anisotropic conditions result in either a cellular, dendritic or planar morphology. As shown in References 30, 31, with decreasing ratio grad T/R a transition from equiaxed to dendritic structures takes place where R is the growth-rate. The fineness of the microstructure is determined by the product grad $T \cdot R$. With increasing grad $T \cdot R$ a finer microstructure solidifies. Due to the change of morphology in the FZ of the square butt welds in the present study, it can be assumed that different grad T/R were present upon solidification of the weld pool. The uniaxial-elongated grains, located in FZ 1 in Figure 13(a), may be caused by higher R combined with a smaller grad T, eventually resulting in a smaller grad T/R ratio than in FZ 2. The higher grad T/R in FZ 2 ultimately leads to a transition from the uniaxial-elongated microstructure to a columnar microstructure. When the boundary between the HAZ and FZ in Reference 23 is studied closely, a transition from equiaxed to columnar grains is evident. Since the uniaxial-elongated grains only occur during MIG welding, it can be assumed that the altered welding process leads to different solidification modes in the FZ.

E. Characterization of the Heat-Treated State

In order to evaluate the impact of the fusion zone on grain growth behavior, a CHT was carried out with specimens welded with a linear energy of $Q = 249$ J mm^{-1}. For the welding with $v = 500$ mm min^{-1}, $v_w = 3$ m min^{-1} and $Q = 249$ J mm^{-1} complete penetration was achieved along with a narrow FZ and HAZ, resulting in a relatively small area influenced by the welding process. Additionally, a high α/γ-ratio in the FZ and HAZ was determined by XRD. A small γ-phase fraction minimizes the impact of non-dissolving γ-phase during CHT, which may result from the change of the minor alloying elements (cf. Figure 8). Furthermore, the weld with $Q = 249$ J mm^{-1} showed the largest major axis of the grains in the FZ, which may lead to a higher grain growth rate of the grains during CHT. After CHT distinct differences in grain size are present between the FZ and the BM [cf. Figure 14(a)]. On the right side from the weld seam, a bamboo-like structure is visible in the BM. The left side even consist of only one abnormal grown grain. In contrast, in the former FZ a polycrystalline microstructure with a nearly homogeneous grain
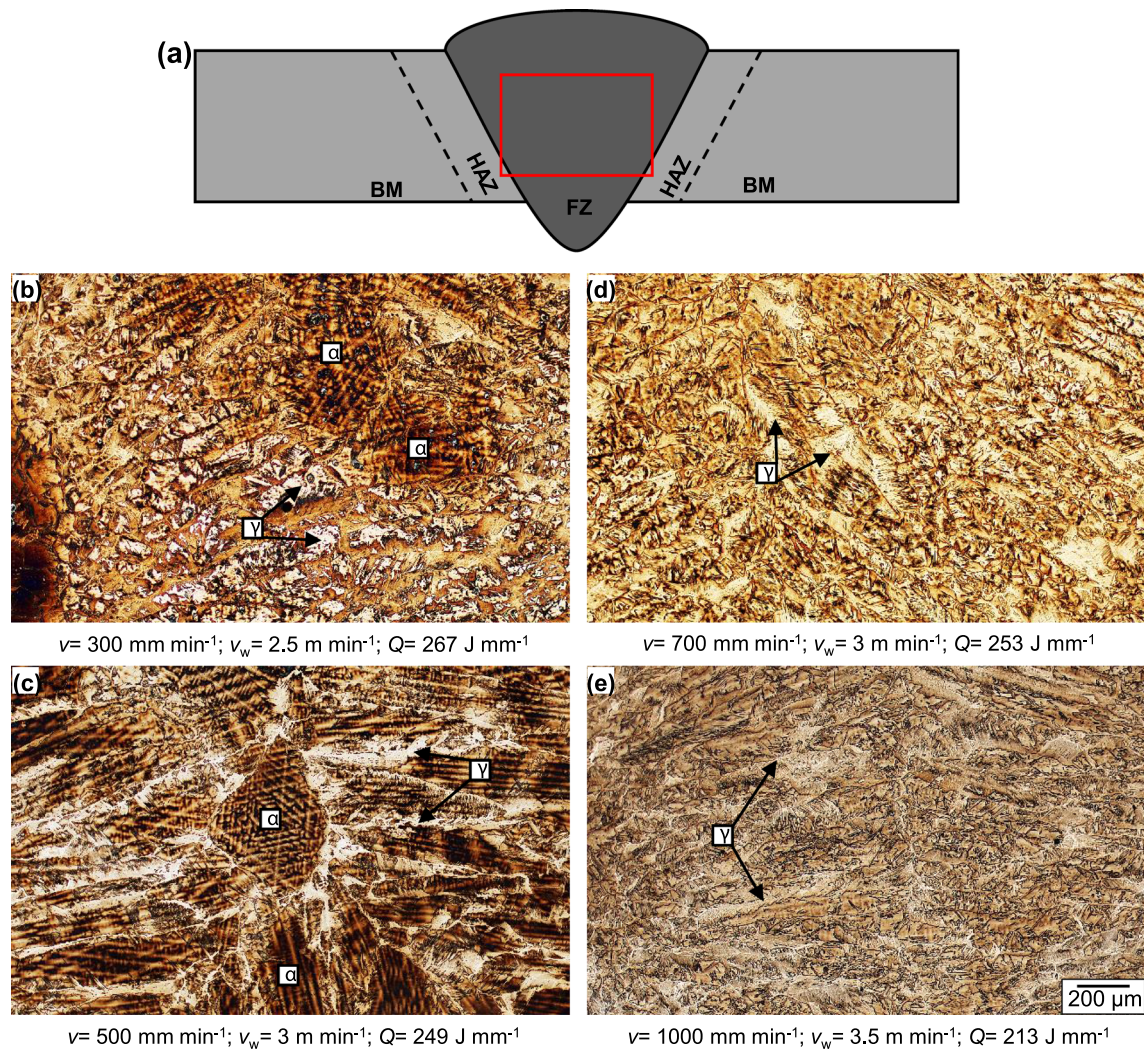
Fig. 9—Microstructure in the FZ: (*a*) schematic overview of the cross-section and position of the micrographs; (*b*) through (*e*) OM of the FZs of the welds with similar filler material and 70/30 Ar/He along with the welding parameters used.

size distribution is present. This illustrates that in the FZ only normal grain growth takes place, while the BM shows AGG. In References 32, 33 the effect of the chemical composition on the grain growth rate is reported. While no loss of the major alloying elements was detected by EDS (*cf*. Figure 7), the measurement of the minor elements by melting gas extraction showed a reduction of the nitrogen content after the welding process. As reported in Reference 34, grain growth kinetics are affected by temperature, specimen size, free-surface energy, texture and pinning of grain boundaries caused by solute atoms or second phase particles. The effect of particles is well-known from fine-grained Al-killed steels. The presence of AlN enables an effective inhibition of normal grain growth at moderate temperatures by pinning the grain boundaries but their coarsening and dissolution lead to AGG at high temperatures.[34] Assuming a similar effect for Fe–Mn–Al–Ni, this might lead to a promoted AGG with an increasing volume fraction of AlN particles. Since the

N content within the FZ is significantly lower than in the BM, it can be assumed that less AlN particles are present. This finally could affect grain growth behavior, resulting in normal grain growth being favored over abnormal grain growth. This assumption is supported by the rapidly changing grain growth rate in the BM and HAZ compared to the FZ, as the AGG is only detected in the BM and HAZ and stopped at the fusion-line. No distinct difference can be observed between the different FZ grain morphologies highlighted in Figure 13. The influence of the grain morphologies in the FZ on AGG can therefore be neglected.

In addition to the chemical composition, the subgrain structures also provides a substantial driving force during the CHT. These are present in the α high-temperature phase after passing through the α + γ two-phase region. The subgrains result from dislocations being induced by the formation and growth of γ-phase during cooling from 1498 K to 1173 K and the subsequent dissolution during heating up to 1498 K.
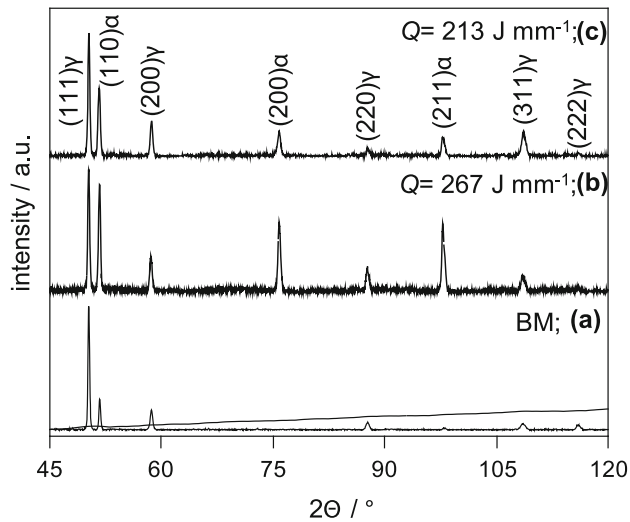
Fig. 10—Diffraction patterns with subtracted background (dotted line in *a*) of the (a) BM and the FZs of the welds with (*b*) $v = 300$ mm min^{-1}, $v_w = 2.5$ m min^{-1}, $Q = 267$ J mm^{-1} and (*c*) $v = 1000$ mm min^{-1}, $v_w = 3.5$ m min^{-1}, $Q = 213$ J mm^{-1}.

Moreover, the driving force for AGG can be increased by a refinement of the subgrain structures caused by a change of chemical composition resulting in a finer γ-phase morphology during CHT.[32,33] In the present case, as shown in Figures 14(b) and (c), the γ-phase morphology after a treatment at 1173 K followed by quenching in cold water does not show any difference between the BM and FZ.

During CHT of Fe–Mn–Al–Ni specimens fused by electron beam welding (EBW), AGG occurs in the FZ as shown earlier.[25] Also, in contrast to the MIG welded specimens in the present study, grain growth across the fusion-line was observable. Still, in some EBW specimens a few smaller grains remained in the former fusion zone. Accordingly, it can be stated that both welding processes have an influence on the AGG, however, their individual impact is different. This may be attributed to the larger melt pool during the MIG process, eventually causing a larger impact due to a more severe loss of minor alloying elements.

As shown for the tensile specimen in Figure 15(a), the hampered AGG in the FZ is not induced by geometric
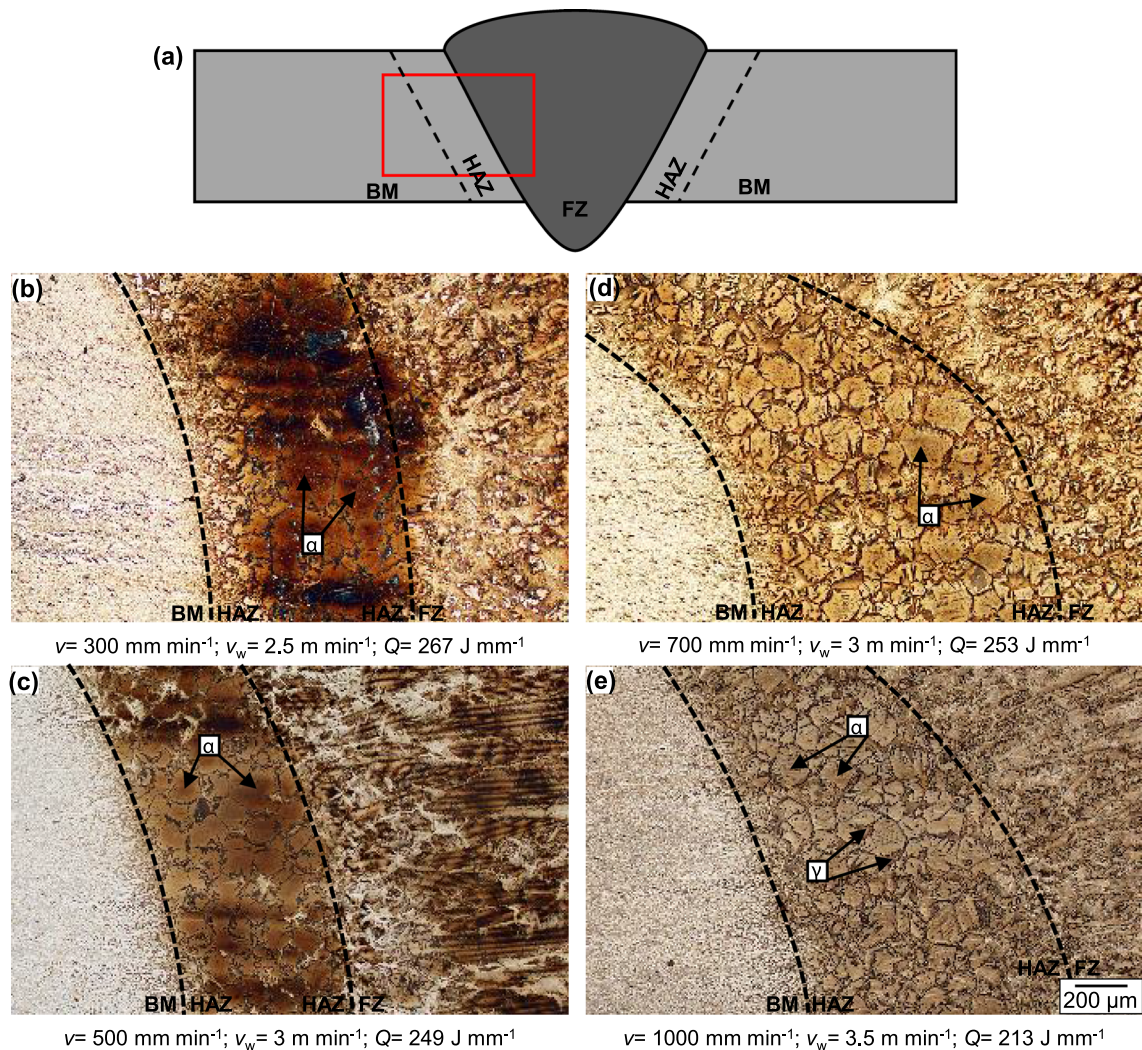

Fig. 11—Microstructure of HAZ: (*a*) schematic overview of the cross-section and position of the micrographs; (*b*) through (*e*) OM of the HAZs of the welds with similar filler material and 70/30 Ar/He along with the welding parameters used.

or surface effects, as the tensile specimen was ground from all sides before the CHT was carried out. By applying an IST, accompanied by OM, the effect of the FZ on the pseudoelastic properties was studied. The stress-strain curve is shown in Figure 15(b). In the first loading cycle up to a strain of 2 pct, the martensitic transformation occurs in the $\langle 114 \rangle$ oriented grain [cf. Figure 15(c)] outside the former FZ. Martensite plates with two differing orientations occur. The interaction of martensite plates with different orientations deteriorate the reversibility of the transformation, as reported in
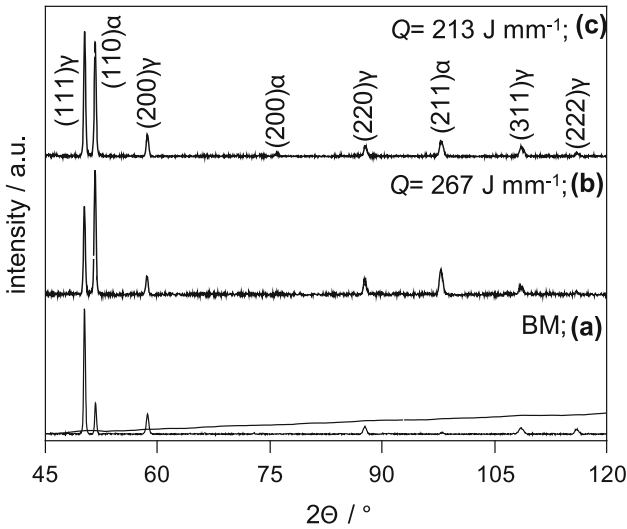
Reference 18. Therefore, a high amount of irreversible strain remains after unloading [Figure 15(d)]. During the second loading cycle up to 4 pct a martensitic transformation within the former FZ takes place [Figure 15(e)]. During the subsequent unloading, only a small amount of retransformation occurs [Figure 15(f)]. Therefore, pseudoelastic strains are hardly visible in the stress-strain curve for the unloading path. At the grain boundaries between the $\langle 114 \rangle$ oriented grain and the polycrystalline structure of the FZ a strong topography has formed, indicating a high amount of plastic deformation resulting from the interaction of the martensite plates with the grain boundaries. During the third loading cycle, martensitic transformation occurs in the $\langle 324 \rangle$ orientated grain. The transformation is accompanied by a decrease of the stress [highlighted in Figure 15(b) with a red arrow]. The martensite formed during loading up to 6 pct strain is visible on the left side of the OM image in Figure 15(g). The subsequent unloading is characterized by a high amount of pseudoelastic strain. This is related to the reversible transformation in the $\langle 324 \rangle$ grain, as the martensite vanishes after unloading [Figure 15(h)]. The pronounced orientation dependent reversibility of the martensitic transformation in Fe–Mn–Al–Ni[15–18] is caused by the anisotropy of the transformation strains[16] and the associated transformation mechanisms.[18] Finally, structural failure occurs in the fourth loading cycle at a strain of 7 pct at the grain boundary between the $\langle 114 \rangle$ and $\langle 316 \rangle$ oriented grain, as shown in Figure 16 by post-mortem OM images of the tensile specimen. As shown in Figure 16(c), the crack is located along the grain boundary between the $\langle 114 \rangle$ and the $\langle 316 \rangle$ orientated grain. In both grains a large fraction of pinned and different orientated martensite plates is present at the mentioned grain boundary. The

Fig. 12—Diffraction patterns with subtracted background (dotted line in a) of the (a) BM and the HAZs of the welds with (b) $v = 300$ mm min^{-1}, $v_w = 2.5$ m min^{-1}, $Q = 267$ J mm^{-1} and (c) $v = 1000$ mm min^{-1}, $v_w = 3.5$ m min^{-1}, $Q = 213$ J mm^{-1}.
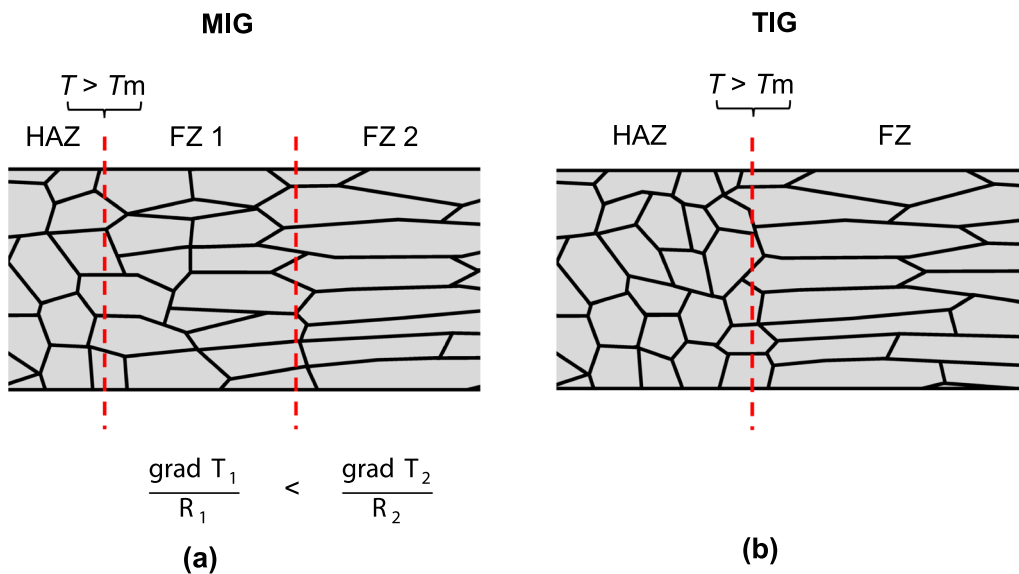

Fig. 13—Grain morphologies upon solidification for (a) MIG and (b) TIG welding (as reported in Ref. [24]); the boundary between the HAZ and the FZ is characterized by temperatures T above the melting point T_m; in (a) the ratio grad T/R in the FZ 1 is smaller than in FZ 2 leading to a change of the solidified microstructure.
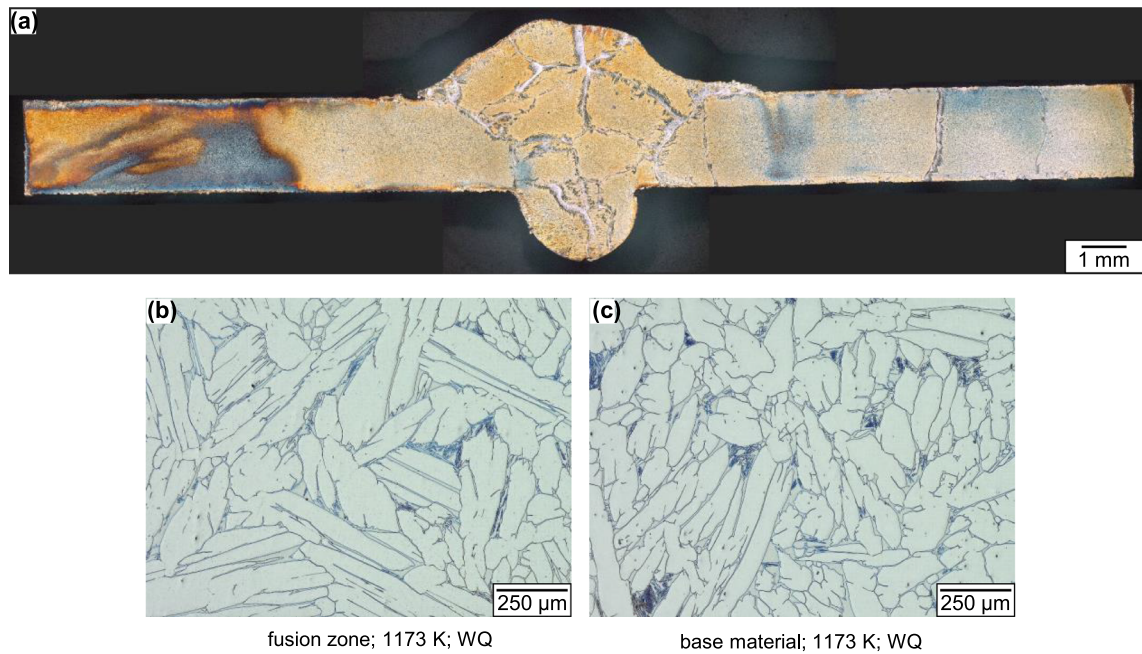
Fig. 14—(a) OM of a polished and etched specimen with $Q = 249$ J mm^{-1} after CHT (quenching by air cooling (AC) with subsequent aging heat treatment at 498 K for 5 h), (b) morphology of γ-phase being present after cold water quenching (WQ) from 1173 K in the FZ and (c) in the BM.

interaction between different orientated martensite plates and the grain boundary leads to stress and strain concentrations which ultimately cause functional failure.[18,35] Severe plastic deformation took also place at the grain boundaries of the former FZ, which is indicated by the topography at Figure 16(b). As shown in Reference 36, the precipitation of the γ-phase takes place predominantly at the grain boundaries. As the γ-phase precipitation is very pronounced in the former FZ, stress can be accommodated by plastic deformation of the ductile γ-phase suppressing structural failure. However, the polycrystalline microstructure affects the pseudoelastic properties, leading to inferior reversibility. Nevertheless, it has to be noted that the influence of the grain orientation of the abnormally grown grains located outside the FZ predominates the pseudoelastic behavior.

IV. CONCLUSIONS

The effect of metal inert gas welding using similar filler material on the microstructure, abnormal grain growth and pseudoelastic properties of industrially processed and hot-rolled Fe–Mn–Al–Ni shape memory alloy sheets was studied. Incremental strain tests of heat-treated welding specimens were carried out and the resulting microstructure was characterized. The main results can be summarized as follows.

(1) While the weld with $Q = 267$ J mm^{-1} shows insufficient penetration, full penetration is achieved with increasing arc power and decreasing mean arc linear energy. In accordance with the penetration the heat-affected zone (HAZ) und fusion zone (FZ) is broader at higher arc power. No cracking was detected in any of the welds.

(2) Line scans showed that no alloying element loss of Fe, Mn, Al or Ni occurred. However, melting gas extraction showed a loss of N for all investigated welds.

(3) The α-phase fraction increases with increasing mean linear arc energy during the metal inert gas welds. While the HAZ is characterized by a major α-phase fraction, the FZ is characterized by a relatively low content of the α-phase. The change in γ precipitation sequence is attributed to the welding process specific temperature-time path and a simultaneous change in the weld pool geometry.

(4) When the grain sizes in the HAZ of all welds are compared, no correlation between grain size and mean arc linear energy can be identified. In contrast, the FZ exhibits for $Q = 249$ J mm^{-1} the largest major axis. Additionally, the FZ can be separated into two distinct zones with different grain morphologies resulting from a change in the grad T/R ratio. However, during cyclic heat treatment abnormal grain growth occurs only in the base metal (BM), while the FZ is characterized by a polycrystalline microstructure.

(5) The polycrystalline microstructure exhibits inferior pseudoelastic properties, as interaction of martensite plates with different orientations deteriorates the reversibility of the transformation. In addition, severe plastic deformation took place in the areas of grain boundaries of the former FZ. However, final failure occurred at a strain of 7 pct along grain boundaries in the BM, where abnormal grain growth had taken place.
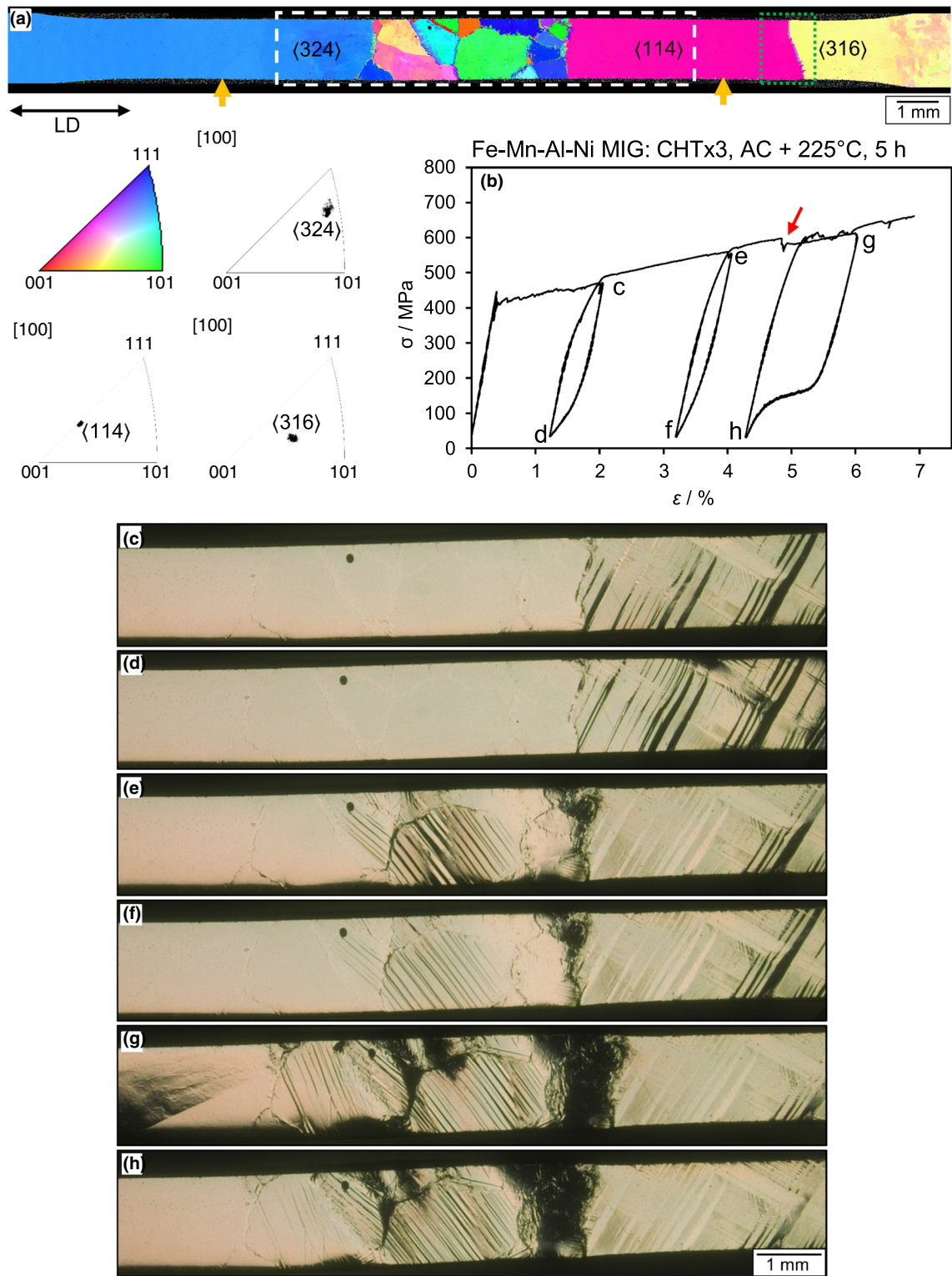
Fig. 15—(a) EBSD orientation map of the cyclic heat-treated tensile specimen (welding parameter Q = 249 J mm^{-1}) used for the IST, the yellow arrows mark the positions of the extensometer, the area shown in the OM images is highlighted with a white dashed box, the grain orientations of the largest grains are shown by the inverse pole figures; (b) stress-strain diagram up to final failure at 7 pct; (c) through (h) OM images at the loading conditions marked in (b) (Color figure online).
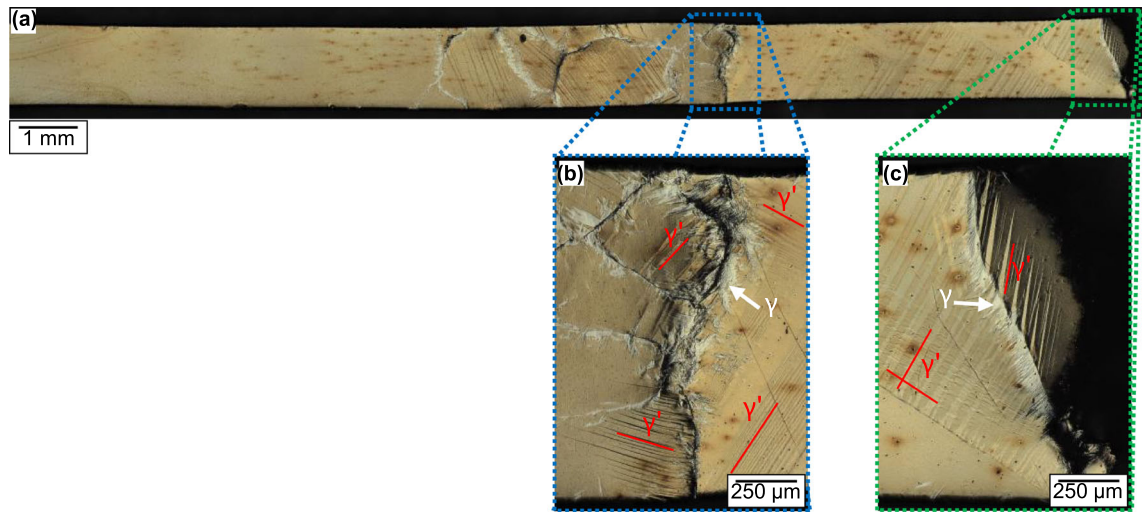
Fig. 16—Post-mortem OM images after final failure: (*a*) overview, (*b*) detailed view on a grain boundary of the former fusion zone, and (*c*) grain boundary causing structural failure in the base material.

AUTHOR CONTRIBUTIONS

VFV: conceptualization, investigation, visualization, writing—original draft preparation. AB: conceptualization, investigation, visualization, writing—original draft preparation. TH (T. Hassel): conceptualization, project administration, writing—review and editing, funding acquisition. TN: writing—review and editing, supervision, funding acquisition. HJM: writing—review and editing, supervision, funding acquisition.

DATA AVAILABILITY

Data are available from the corresponding author on request.

CONFLICT OF INTEREST

The authors declare that they have no conflict of interest.

REFERENCES

1. A. Abbass, R. Attarnejad, and M. Ghassemieh: *Materials*, 2020, vol. 13, p. 1701.
2. S. Li, F. Hedayati Dezfuli, J. Wang, and M.S. Alam: *J. Intell. Mater. Syst. Struct.*, 2020, vol. 31, pp. 1053–75.
3. M. Vollmer, A. Bauer, J.-M. Frenck, P. Krooß, A. Wetzel, B. Middendorf, E. Fehling, and T. Niendorf: *Eng. Struct.*, 2021, vol. 241, p. 112430.
4. T. Omori, K. Ando, M. Okano, X. Xu, Y. Tanaka, I. Ohnuma, R. Kainuma, and K. Ishida: *Science*, 2011, vol. 333, pp. 68–71.
5. T. Omori, H. Iwaizako, and R. Kainuma: *Mater. Des.*, 2016, vol. 101, pp. 263–69.
6. M. Vollmer, A. Bauer, M.J. Kriegel, M. Motylenko, and T. Niendorf: *Scripta Mater.*, 2021, vol. 194, p. 113619.
7. T. Omori, M. Okano, and R. Kainuma: *APL Mater.*, 2013, vol. 1, p. 32103.
8. Y. Sutou, T. Omori, K. Yamauchi, N. Ono, R. Kainuma, and K. Ishida: *Acta Mater.*, 2005, vol. 53, pp. 4121–33.
9. Y. Sutou, T. Omori, R. Kainuma, and K. Ishida: *Acta Mater.*, 2013, vol. 61, pp. 3842–50.

10. S.M. Ueland, Y. Chen, and C.A. Schuh: *Adv. Funct. Mater.*, 2012, vol. 22, pp. 2094–99.
11. S.M. Ueland and C.A. Schuh: *Acta Mater.*, 2012, vol. 60, pp. 282–92.
12. S.M. Ueland and C.A. Schuh: *J. Appl. Phys.*, 2013, vol. 114, p. 53503.
13. J.-X. Xie, J.-L. Liu, and H.-Y. Huang: *Rare Met.*, 2015, vol. 34, pp. 607–24.
14. T. Omori, T. Kusama, S. Kawata, I. Ohnuma, Y. Sutou, Y. Araki, K. Ishida, and R. Kainuma: *Science*, 2013, vol. 341, pp. 1500–02.
15. L.W. Tseng, J. Ma, S.J. Wang, I. Karaman, M. Kaya, Z.P. Luo, and Y.I. Chumlyakov: *Acta Mater.*, 2015, vol. 89, pp. 374–83.
16. L.W. Tseng, J. Ma, S.J. Wang, I. Karaman, and Y.I. Chumlyakov: *Scripta Mater.*, 2016, vol. 116, pp. 147–51.
17. L.W. Tseng, J. Ma, Y.I. Chumlyakov, and I. Karaman: *Scripta Mater.*, 2019, vol. 166, pp. 48–52.
18. A. Bauer, M. Vollmer, and T. Niendorf: *Shape Mem. Superelast.*, 2021, vol. 7, pp. 373–82.
19. T. Niendorf, F. Brenne, P. Krooß, M. Vollmer, J. Günther, D. Schwarze, and H. Biermann: *Metall. Mater. Trans. A*, 2016, vol. 47A, pp. 2569–73.
20. P. Krooß, J. Günther, L. Halbauer, M. Vollmer, A. Buchwalder, R. Zenker, H. Biermann, and T. Niendorf: *Funct. Mater. Lett.*, 2017, vol. 10, p. 1750043.
21. M. Vollmer, D. Baunack, D. Janoschka, and T. Niendorf: *Shape Mem. Superelast.*, 2020, vol. 6, pp. 131–38.
22. F.C. Ewald, F. Brenne, T. Gustmann, M. Vollmer, P. Krooß, and T. Niendorf: *Metals*, 2021, vol. 11, p. 185.
23. V.F. Viebranz, T. Hassel, T. Niendorf, and H.J. Maier: *Weld. World*, 2022, vol. 66, pp. 2207–16.
24. V.F. Viebranz, T. Hassel, and H.J. Maier: *Metals*, 2022, vol. 12, p. 1731.
25. A. Bauer, M. Wiegand, P. Wicke, N. Sommer, M. Vollmer, S. Böhm, and T. Niendorf: *Shape Mem. Superelast.*, 2023, vol. 9, pp. 364–76.
26. L.V. Hölscher, T. Hassel, and H.J. Maier: *Int. J. Adv. Manuf. Technol.*, 2022, vol. 120, pp. 989–99.
27. J. Schindelin, I. Arganda-Carreras, E. Frise, V. Kaynig, M. Longair, T. Pietzsch, S. Preibisch, C. Rueden, S. Saalfeld, B. Schmid, J.-Y. Tinevez, D.J. White, V. Hartenstein, K. Eliceiri, P. Tomancak, and A. Cardona: *Nat. Methods*, 2012, vol. 9, pp. 676–82.
28. V.A. Hosseini, S. Wessman, K. Hurtig, and L. Karlsson: *Mater. Des.*, 2016, vol. 98, pp. 88–97.
29. L. Wang, Y. Li, J. Ding, Q. Xie, X. Zhang, and K. Wang: *Metals*, 2022, vol. 12, p. 1273.
30. D.M. Stefanescu, and R. Ruxanda: *Fundamentals of Solidification, ASM Handbook Vol. 9—Metallography and Microstructures*, ASM International, 2004, pp. 71–92.
31. W. Kurz and D.J. Fisher: *Fundamentals of Solidification*, 4th ed. Trans Tech Publications, Uetikon-Zuerich, Switzerland, 1998, pp. 67–108.
32. M. Vollmer, T. Arold, M.J. Kriegel, V. Klemm, S. Degener, J. Freudenberger, and T. Niendorf: *Nat. Commun.*, 2019, vol. 10, p. 2337.
33. J. Xia, T. Omori, and R. Kainuma: *Scripta Mater.*, 2020, vol. 187, pp. 355–59.
34. F. Najafkhani, S. Kheiri, B. Pourbahari, and H. Mirzadeh: *Arch. Civ. Mech. Eng.*, 2021, vol. 21, pp. 1–20.
35. W. Abuzaid, Y. Wu, R. Sidharth, F. Brenne, S. Alkan, M. Vollmer, P. Krooß, T. Niendorf, and H. Sehitoglu: *Shape Mem. Superelast.*, 2019, vol. 5, pp. 263–77.
36. M. Vollmer, C. Segel, P. Krooß, J. Günther, L.W. Tseng, I. Karaman, A. Weidner, H. Biermann, and T. Niendorf: *Scripta Mater.*, 2015, vol. 108, pp. 23–26.